Yang, Y., Zheng, Y., Chen, J., Zhou, S., Celyan, S., Sandvol, E., Tilmann, F., Priestley, K., Hearn, T. M., Ni, J. F., Broewn, L. D., Ritzwoller, M. H. (2010): Rayleigh wave phase velocity maps of Tibet and the surrounding regions from ambient seismic noise tomography. - Geochemistry Geophysics Geosystems (G3), 11, Q08010

DOI: 10.1029/2010GC003119

Geochemistry Geophysics Geosystems G3

Article
Volume 11, Number 8
6 August 2010
Q08010, doi:10.1029/2010GC003119
ISSN: 1525-2027

Published by AGU and the Geochemical Society

Rayleigh wave phase velocity maps of Tibet and the surrounding regions from ambient seismic noise tomography

Yingjie Yang
Center for Imaging the Earth's Interior, Department of Physics, University of Colorado at Boulder, Boulder, Colorado 80309-0390, USA

Key Laboratory of Dynamic Geodesy, Institute of Geodesy and Geophysics, Chinese Academy of Sciences, Wuhan 430077, China (yingjie.yang@colorado.edu)

Yong Zheng
Key Laboratory of Dynamic Geodesy, Institute of Geodesy and Geophysics, Chinese Academy of Sciences, Wuhan 430077, China

John Chen and Shiyong Zhou
Institute of Theoretical and Applied Geophysics, School of Earth and Space Sciences, Peking University, Beijing 100871, China

Savas Celyan and Eric Sandvol
Department of Geological Sciences, University of Missouri, Columbia, Missouri 65211, USA

Frederik Tilmann
Department of Earth Sciences, University of Cambridge, Cambridge CB3 0EZ, UK

Helmholtz-Zentrum Potsdam, Deutsches GeoForschungsZentrum, D-14473 Potsdam, Germany

Keith Priestley
Department of Earth Sciences, University of Cambridge, Cambridge CB3 0EZ, UK

Thomas M. Hearn and James F. Ni
Department of Physics, New Mexico State University, Las Cruces, New Mexico 88003, USA

Larry D. Brown
Earth and Atmospheric Sciences, Cornell University, Ithaca, New York 14853, USA

Michael H. Ritzwoller
Center for Imaging the Earth's Interior, Department of Physics, University of Colorado at Boulder, Boulder, Colorado 80309-0390, USA

[1] Ambient noise tomography is applied to the significant data resources now available across Tibet and surrounding regions to produce Rayleigh wave phase speed maps at periods between 6 and 50 s. Data resources include the permanent Federation of Digital Seismographic Networks, five temporary U.S. Program for Array Seismic Studies of the Continental Lithosphere (PASSCAL) experiments in and around Tibet, and Chinese provincial networks surrounding Tibet from 2003 to 2009, totaling ~600 stations and ~150,000 interstation

paths. With such a heterogeneous data set, data quality control is of utmost importance. We apply conservative data quality control criteria to accept between ~5000 and ~45,000 measurements as a function of period, which produce a lateral resolution between 100 and 200 km across most of the Tibetan Plateau and adjacent regions to the east. Misfits to the accepted measurements among PASSCAL stations and among Chinese stations are similar, with a standard deviation of ~1.7 s, which indicates that the final dispersion measurements from Chinese and PASSCAL stations are of similar quality. Phase velocities across the Tibetan Plateau are lower, on average, than those in the surrounding nonbasin regions. Phase velocities in northern Tibet are lower than those in southern Tibet, perhaps implying different spatial and temporal variations in the way the high elevations of the plateau are created and maintained. At short periods (<20 s), very low phase velocities are imaged in the major basins, including the Tarim, Qaidam, Junggar, and Sichuan basins, and in the Ordos Block. At intermediate and long periods (>20 s), very high velocities are imaged in the Tarim Basin, the Ordos Block, and the Sichuan Basin. These phase velocity dispersion maps provide information needed to construct a 3-D shear velocity model of the crust across the Tibetan Plateau and surrounding regions.

Components: 8600 words, 14 figures, 1 table.

Keywords: ambient noise; Rayleigh wave; tomography; Tibet.

Index Terms: 7255 Seismology: Surface waves and free oscillations (6982); 7270 Seismology: Tomography (6982); 7205 Seismology: Continental crust (1219).

Received 4 March 2010; **Revised** 23 April 2010; **Accepted** 30 April 2010; **Published** 6 August 2010.

Yang, Y., et al. (2010), Rayleigh wave phase velocity maps of Tibet and the surrounding regions from ambient seismic noise tomography, *Geochem. Geophys. Geosyst.*, *11*, Q08010, doi:10.1029/2010GC003119.

1. Introduction

[2] Ambient noise tomography based on cross correlations of long recordings of seismic noise data observed between pairs of stations has proven to be a powerful method to construct surface wave dispersion maps at short and intermediate periods. These surface wave maps provide constraints on crustal structure, which were difficult to obtain from traditional earthquake surface wave tomography due to the strong attenuation and scattering at short periods at teleseismic distances.

[3] Since the first ambient noise tomographic images of Rayleigh wave group speeds in the microseismic band from 5 to 20 s appeared in 2004 [*Sabra et al.*, 2005; *Shapiro et al.*, 2005] for southern California based on the earliest data from the EarthScope Transportable Array (TA), this method has become increasingly widespread because of its unique ability to constrain crustal structure independent of earthquakes or human-made explosions. Ambient noise tomography has now been applied around the world to image crustal structures, including at regional scales in New Zealand [*Lin et al.*, 2007], Southern Africa [*Yang et al.*, 2008a], Spain [*Villaseñor et al.*, 2007], Korea [*Cho et al.*, 2007], Japan [*Nishida et al.*, 2008], and the western U.S. [*Moschetti et al.*, 2007; *Lin et al.*, 2008; *Yang et al.*, 2008b] and at continental scales across Europe [*Yang et al.*, 2007], China [*Zheng et al.*, 2008], the USA [*Bensen et al.*, 2008, 2009], Australia [*Saygin and Kennett*, 2010] as well as other places.

[4] Across Tibet and the surrounding regions, numerous global-scale teleseismic earthquake studies of surface wave dispersion have been performed [e.g., *Levshin et al.*, 1994; *Ritzwoller and Levshin*, 1998; *Ritzwoller et al.*, 1998; *Villaseñor et al.*, 2001; *Friederich*, 2003; *Huang et al.*, 2003; *Shapiro et al.*, 2004; *Levshin et al.*, 2005b; *Priestley et al.*, 2006]. In addition, several regional-scale studies based on ambient noise tomography have already been carried out in southeastern Tibet [*Yao et al.*, 2006, 2008], southern Tibet [*Guo et al.*, 2009], and in western Sichuan and eastern Tibet [*Li et al.*, 2009]. The regional studies have all generated high-resolution crustal models at regional scales. One velocity feature that has been inferred by several researchers in southern Tibet is a low-velocity zone (LVZ) in the middle crust [*Cotte et al.*, 1999; *Rapine et al.*, 2003; *Caldwell et al.*, 2009], which appears to support the crustal flow model proposed by *Royden et al.* [1997] and *Nelson et al.* [1996] that predicts decoupling of the upper crustal

deformation from the motion of the underlying mantle. However, as shown by H. Yao et al. (Heterogeneity and anisotropy of the lithosphere of SE Tibet from ambient noise and surface wave array analysis, submitted to *Journal of Geophysical Research*, 2010), LVZs in the middle and lower crust beneath southeastern Tibet appear to form complex 3-D structures with substantial lateral variations in depth, thickness, and strength of velocity anomalies. The lateral and vertical variations of LVZs raise questions, such as, whether the low-velocity zones are present ubiquitously across all of Tibet and if they interconnect to form flowable channels or are isolated and concentrated only in certain areas of Tibet.

[5] To address questions associated with middle and lower crustal flow and interpret crustal structures in the context of larger-scale structures, an integrated crustal velocity model is needed. Recently, using data from 47 stations of the China National Seismic Network and 12 other global stations in adjacent regions, large-scale group velocity maps at periods from 8 to 60 s have been generated by *Zheng et al.* [2008] across all of China. However, due to the limitations imposed by station number and distribution, most of raypaths lie in eastern China and resolution in Tibet is not high enough to detect detailed lateral variations within the crust.

[6] In the past few years, several Program for Array Seismic Studies of the Continental Lithosphere (PASSCAL) experiments have been carried out in Tibet. Meanwhile, numerous Chinese provincial networks in Tibet and surrounding areas have been updated to intermediate-band stations and seismic waveforms from these networks have been archived continuously. In this study, we assemble all stations from the PASSCAL experiments operated between years 2003 and 2009 as well as stations from the Chinese Provincial Networks from August 2007 to July 2009, with the number of stations totaling approximately 600. The details of these networks are described in section 2. The large number of stations provides unprecedented coverage over the Tibetan Plateau and also extends east of the plateau. Based on cross correlations of the continuous data from these stations, we obtain Rayleigh phase velocity dispersion measurements at periods from 6 to 50 s which are then used to generate phase velocity maps with resolution on the order of 100–200 km. The focus of this paper is on the acquisition and quality control of the data set itself, on the ambient noise cross correlations and dispersion measurements, and the production of the Rayleigh wave phase velocity maps. Love wave maps, assimilation of teleseismic data, and inversion for 3-D isotropic and anisotropic structures will be subjects of later contributions.

2. Data Acquisition and Quality Control

[7] The data used in this study are continuous seismic waveforms recorded at broadband stations that exist in and around Tibet from years 2003–2005 and 2007–2009 from the following networks: (1) five PASSCAL experiments (Namche Barwa, HI-CLIMB, MIT-CHINA, INDEPTH IV, western Tibet), (2) Chinese Provincial Networks in and around Tibet, and (3) Federation of Digital Seismographic Networks (FDSN) stations (e.g., GSN, GEOSCOPE, GEOFON) and regional networks (KZ and KN) within and around the region of study. Figure 1 and Table 1 summarize these data sets. In total, we process data from approximately 600 stations of which about 250 are from the Chinese Provincial Networks. The operating times of the five PASSCAL experiments are listed in Table 1 along with the Chinese Provincial stations. In Table 1, the overlap in time of two experiments, which is a necessary requirement for cross correlation of ambient noise, is marked with a cross. Blanks in Table 1 indicate no temporal overlap between a pair of experiments. For example, the three PASSCAL experiments that operated in the period of 2003–2005 overlap each other. The INDEPTH IV and western Tibet experiments in 2007–2009 also overlap each other and the entire Chinese Provincial Networks. These overlaps guarantee that dense ray coverage is generated in this study. Cross correlations with longer time series result in higher SNR surface waves. Previous studies in Europe [*Yang et al.*, 2007] and the US [*Bensen et al.*, 2008] found that several months of continuous seismic data are required to obtain high SNR cross correlations. The time spans of overlap between different networks in this study are typically longer than 1 year, which allows the high SNR cross correlations between different networks to be obtained.

[8] Because the stations used in this study have different types of seismometers, especially among the Chinese stations, significant effort must be devoted to data quality control. The most critical aspect in ambient noise tomography is consistency and accuracy of timing between different networks. Because data from Chinese stations are recorded in Beijing Time, we first correct all the recording times to Greenwich Mean Time (GMT). We then remove instrument responses from all continuous waveforms, which is necessary to unify the frequency-dependent timings recorded at different types of

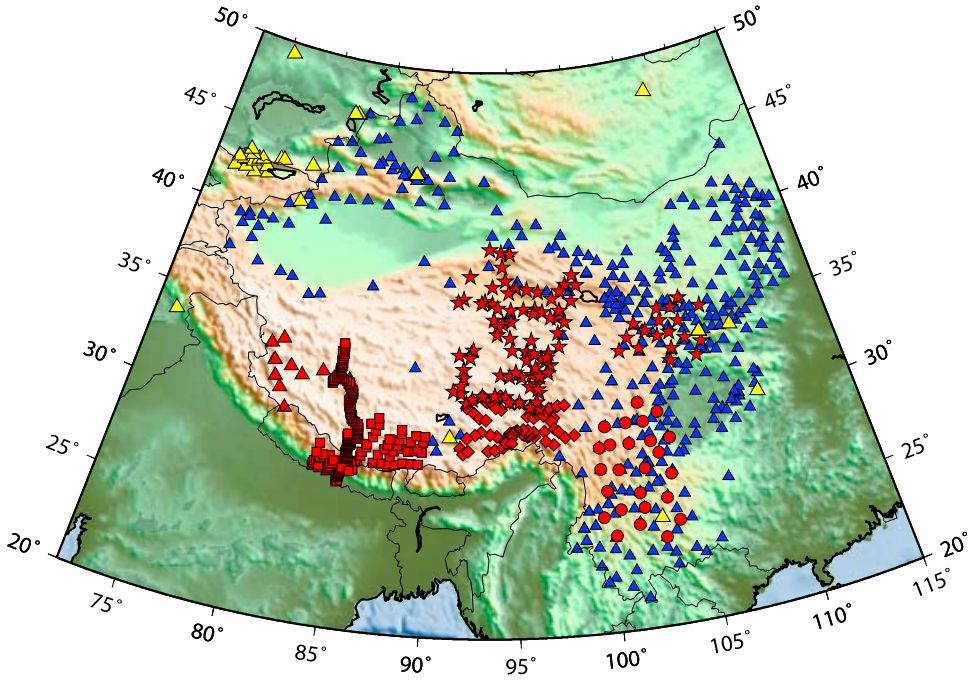

Figure 1. Station coverage in and around Tibet between 2003 and 2009. Symbols are defined in Table 1. Red symbols represent PASSCAL stations, blue triangles represent Chinese Provincial stations, and yellow triangles are FDSN and other regional networks. Concurrent installations are indicated by crosses in Table 1.

seismometers. However, we found a difference in the format of the response files between the PASSCAL stations and the Chinese stations. In the response files of the PASSCAL stations, one additional pole was added to the original response files, which was intended to convert velocity data to displacement data. On the other hand, in the response files of the Chinese stations, the original response files of the seismometers are kept, which means the waveforms of Chinese stations after instrument response removal have units of velocity. To ensure the consistency of the data, we added an additional pole to individual response files of the Chinese stations, which converted all data to displacement.

[9] Figure 2 illustrates the problem of inconsistent response files by showing the cross correlation between PASSCAL station GS02 (from the INDEPTH IV experiment) and Chinese station SNT, which have an interstation distance of 637 km. When applying the original uncorrected response files for the Chinese station, the negative component of the cross correlation (red traces) and the positive component (black traces) are inverted in sign relative to each other in the time windows of the surface wave signals (Figure 2b). This results from the $\pi/2$ phase difference between velocity and displacement, which produces a phase difference of π between the positive and negative lags of cross

Table 1. Broadband Seismic Networks Installed During 2003–2009 in and Around Tibet

Network (Network Code)	Approximate Operation Time	Symbol in Figure 1	Network Code[a] XE (71)	YA (25)	XF (200)	X4 (97)	Y2 (9)	CPN (~250)	FDSN (33)
Namche Barwa (XE)	Jul 2003 to Oct 2004	red diamond	X	X	X				X
MIT-China (YA)	Sep 2003 to Sep 2004	red circle		X	X				X
Hi-CLIMB (XF)	Sep 2002 to Aug 2005	red square			X				X
INDEPTH IV (X4)	May 2007 to May 2009	red star				X	X	X	X
Western Tibet (Y2)	Jul 2007 to Aug 2008	red triangle					X	X	X
Chinese Provincial Network (CPN)	May 2007 to May 2009	blue triangle						X	X
FDSN and regional (G, PS, IC, II, IU, KZ, and KN)		yellow triangle							X

[a]The number of stations of each PASSCAL experiment is indicated in parentheses following the relevant network code. The crosses indicate stations deployed concurrently.

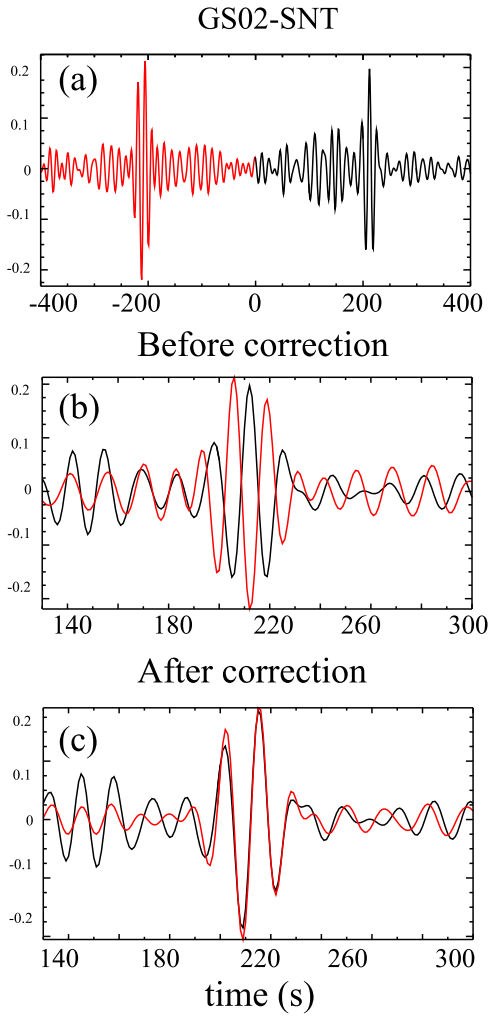

Figure 2. (a) A cross correlation between PASSCAL station GS02 and Chinese station SNT with an interstation distance of 637 km. The red trace is the negative lag component, and the black trace is the positive lag component. (b and c) Comparison between positive and negative components before and after correcting the instrument response file of the Chinese station SNT. Note that the two components are inverted before the correction, which converts the Chinese waveform to displacement.

correlations. Upon adding one additional pole in the response files of the Chinese stations, equivalent to converting all waveforms to displacement, the surface wave signals on the two components are nearly identical (Figure 2c). This is as expected because the two components represent surface waves propagating in opposite directions but sensing the same medium between the two stations.

[10] After removing instrument responses from the waveforms using consistent response files, we then check the vertical polarities of all stations by comparing the waveforms of first P arrivals from large teleseismic events. We find all PASSCAL stations and Chinese stations in this study have vertical polarizations consistent with the FDSN stations. Furthermore, we check for possible timing errors for each station using two methods. First, we compare the two-sided arrivals of interstation cross correlation, as shown in Figure 2. If one station has a timing error, the resulting difference of arrival times of surface wave signals between the positive and negative components will be twice the error; otherwise it will be nearly zero. This method was used to detect station timing errors in California by *Stehly et al.* [2007]. However, because strong noise energy usually comes from coastlines and noise energy attenuates when propagating inland [e.g., *Yang and Ritzwoller*, 2008], surface wave signals from a cross correlation are typically not symmetric. In some cases only one component has a high signal-to-noise ratio (SNR), which renders this method invalid. The second method to check for timing errors is performed during tomography. First, we create a somewhat overly smoothed tomographic map to avoid generating local phase velocity anomalies introduced by timing errors at a station. After the tomography, we calculate average misfit of travel times for each station. Because each station has numerous interstation phase velocity measurements with other stations and the bearings of the corresponding interstation paths align in various azimuthal directions, the average misfit should be very close to zero. We discard stations with average misfits larger than 5 s. The number of stations discarded in this step is only 15, small compared to the total number of stations (~600). All of those stations are Chinese stations except for one station from the INDEPTH IV experiment, C11, with a dysfunctional GPS clock.

3. Data Processing and Selection

[11] The data processing procedures we adopt here follow those of *Bensen et al.* [2007] except in one step: temporal normalization. In the work by *Bensen et al.* [2007], a running absolute mean normalization is applied to seismic waveforms to suppress the effects of earthquakes, instrumental irregularities and nonstationary noise sources near to stations on cross correlations, while still retaining some aspects of the amplitude information of the noise. This method computes the running average of the absolute values of waveforms in a normalization time window of fixed length and weights waveforms by the inverse of these averages. We apply this same temporal normalization to data from PASSCAL stations and

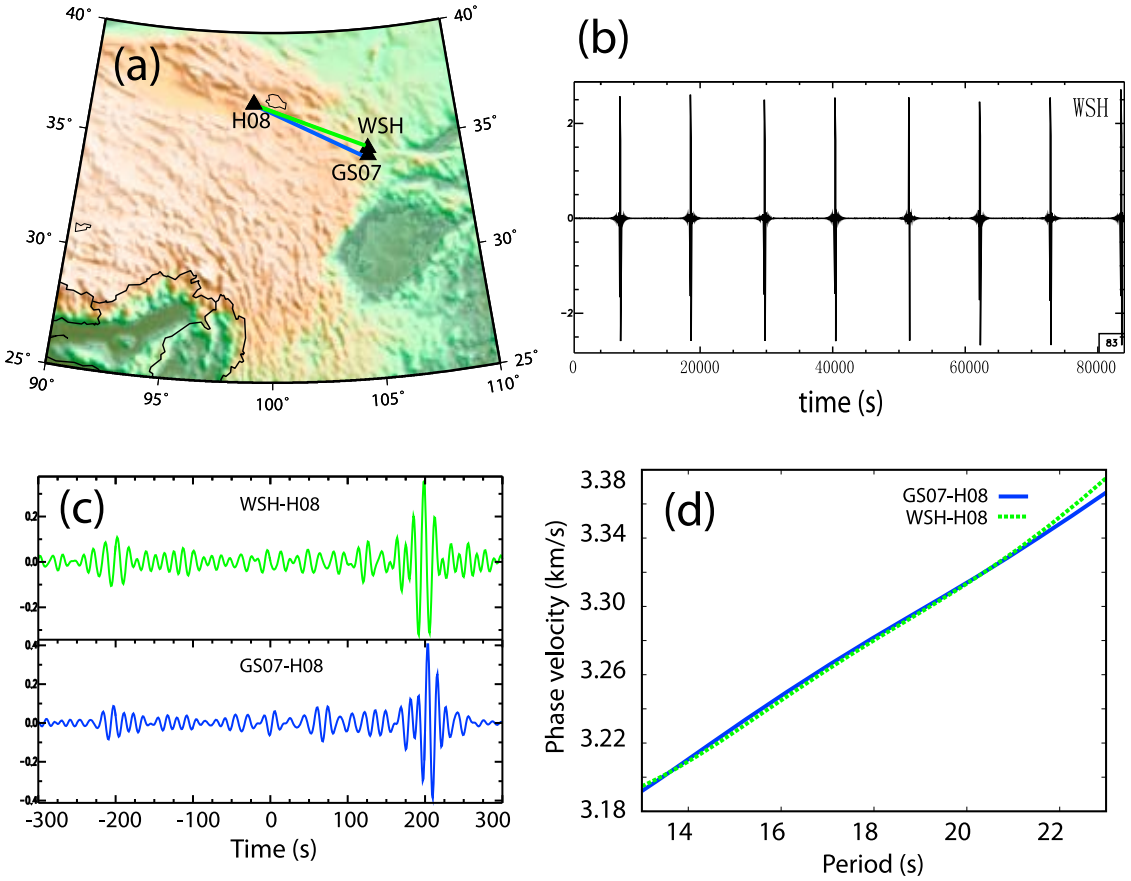

Figure 3. Comparison of two cross correlations, one between two PASSCAL stations H08 and GS07 and the other between the same PASSCAL station H08 and a Chinese station WSH. The raw waveform from the Chinese station WSH possessed spikes of unknown origin. (a) The three black triangles denote the locations of the three stations with the blue line connecting H08 and GS07 and the green line connecting H08 and WSH. (b) One day time series from station WSH on 20 January 2009. (c and d) Cross correlations between WSH-H08 and GS07-H08 and the corresponding phase velocity dispersion measurements, showing that the data irregularities of station WSH do not deteriorate dispersion information within the cross correlations.

FDSN stations. However, for some Chinese stations (e.g., Figure 3a), there are unusual spikes and irregularities in the waveforms such as the example for the station WSH shown in Figure 3b. For this kind of waveform, we find that the running absolute mean normalization does not remove these spikes and irregularities. Instead, we apply one-bit normalization to all Chinese stations to suppress the effects of the spikes by keeping only phase information. For example, Figure 3c shows the comparison of two cross correlations, one between the two PASSCAL stations H08 and GS07 and the other between the common PASSCAL station H08 and a Chinese station WSH. The PASSCAL station GS07 and the Chinese station WSH are located very close to one other. The waveforms of surface wave signals from cross correlations and the resulting phase velocity dispersion measurements are quite similar, as shown in Figures 3c and 3d, even though the Chinese and PASSCAL waveforms have been normalized in time differently.

[12] In this study, we only process vertical component ambient noise, so that the cross correlations predominantly contain only Rayleigh wave signals. We filter the data at periods between 4 and 60 s before applying time domain normalization. Figure 4 presents examples of cross-correlation record sections between some PASSCAL and Chinese stations and among the Chinese stations. The time series lengths in cross correlations range from 1 to 2 years in duration. Strong surface wave signals are seen for both positive and negative correlation lags with an average moveout velocity of 3 km/s. To simplify data analysis and enhance the SNR of the surface waves, we separate each cross correlation into positive and negative lag components and then add the two components to form the so-called

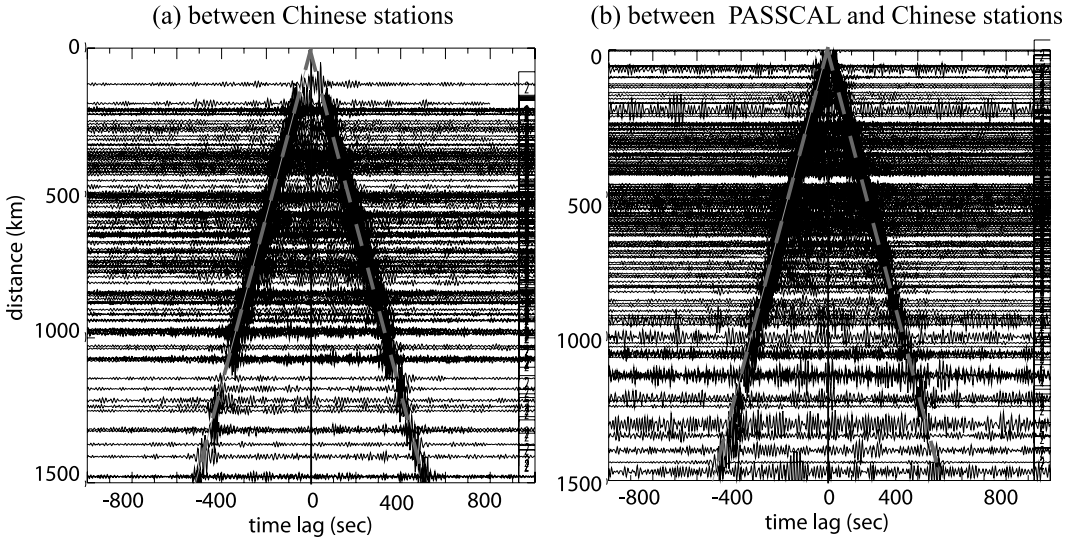

Figure 4. Record sections of cross correlations obtained from about 1 year of waveform data (a) between Chinese provincial network stations and (b) between the Chinese stations and PASSCAL stations. The gray dash lines display a moveout of 3 km/s.

"symmetric component." All subsequent analysis is performed on the symmetric components.

[13] After obtaining all interstation cross correlations, we calculate the period-dependent signal-to-noise (SNR) from the symmetric components. SNR is defined as the ratio of the peak amplitude within a time window containing the surface wave signals to the root-mean-square of the noise trailing the signal arrival window. Figure 5 presents the average SNR as a function of period for cross correlations among PASSCAL stations (red lines), among Chinese stations (blue lines), and between PASSCAL stations and Chinese stations (black lines), segregated into three interstation distance ranges: three wavelengths to 500 km, 500–1000 km, and 1000–1500 km. SNR is higher for cross correlations between PASSCAL stations than between Chinese stations at all periods and distance ranges, and is similar for cross correlations between Chinese stations and between Chinese and PASSCAL stations. Data quality from Chinese stations, therefore, is lower than that from PASSCAL stations, consistent with the observations of the unusual spikes and irregularities that affect some of the Chinese network. The patterns of SNR as a function of period are similar for measurements from both PASSCAL and Chinese stations. SNR is highest at the microseism band (5–20 s). The peak SNR is around 15 s, at the center of the primary microseism band (10–20 s), which is consistent with ambient noise studies in the USA [e.g., *Bensen et al.*, 2008]. SNR decreases with interstation distance (Figures 5a–5c) due to scattering and attenuation. The SNR difference between the PASSCAL and Chinese stations is relatively greatest at the longer periods because the instrument response for many of the Chinese stations rolls off more rapidly above ~25 s period.

[14] After obtaining all cross correlations and calculating SNR, three selection criteria are applied prior to tomography. The number of measurements remaining after each selection step is plotted in Figure 6, segregated by measurements among PASSCAL stations (Figure 6a) and among Chinese stations (Figure 6b). First, we accept measurements only when the distance between the two stations is greater than three wavelengths. The total number of measurements rejected by this criterion is ~10% at short periods, but increases to ~20% at long periods. For example, the wavelength of Rayleigh wave at 50 s period is ~160 km, which requires interstation distances longer than 480 km. Second, we use SNR to select acceptable measurements. At individual periods, only those measurements with SNR higher than 15 are accepted. This criterion rejects more than half of all measurements. In particular, more than 90% of the measurements from Chinese stations at periods longer than 30 s are rejected, because the Chinese seismometers have a corner period of 30 s at the long-period end. Third, we require that the dispersion measurements agree with one another across the data set; that is, most of the measurements should be able to be fit well during tomography. This

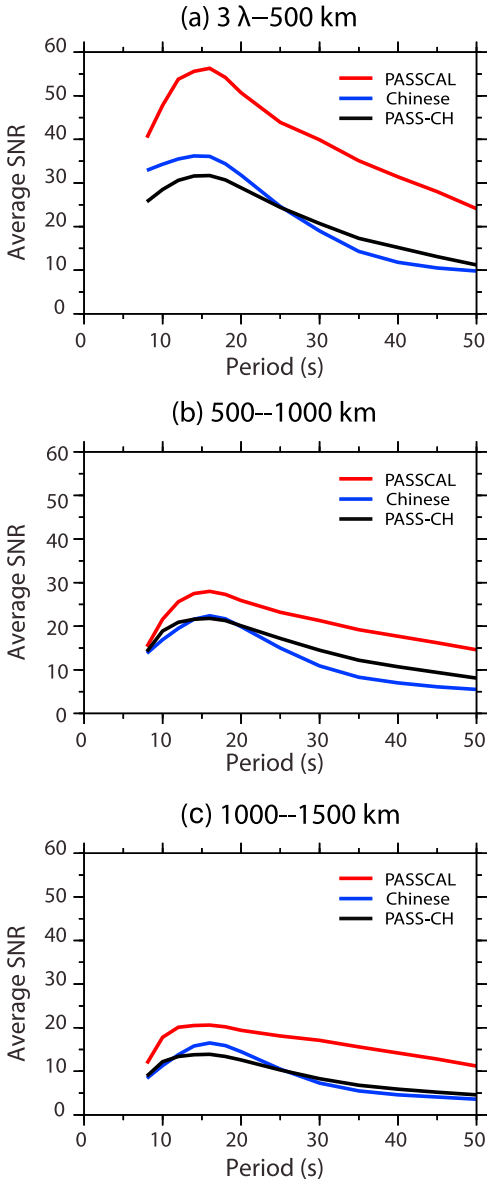

Figure 5. Average SNR as a function of period for cross correlations among PASSCAL stations (red lines), among Chinese stations (blue lines), and between PASSCAL stations and Chinese stations (black lines), segregated by interstation distance: (a) three wavelengths to 500 km, (b) 500–1000 km, and (c) 1000–1500 km.

condition is applied during tomography. This last step rejects a small portion of data, typically less than 5% of the number remaining after the second step. We finally obtain between ~5000 and ~45000 phase speed measurements as a function of period from 6 to 50 s (Figure 7). The number of measurements reaches a maximum between periods of 10 and 20 s, i.e., in the primary microseismic band, and then decreases with period so that at 50 s there are only about 5000 measurements.

[15] The azimuthal distributions of SNR (Figures 8a–8c) and number of paths (Figures 8d–8f) of the selected measurements at 16 s period are plotted in Figure 8, segregated into station groups: PASSCAL stations, Chinese stations, and all stations. The azimuthal distribution at other periods is similar to the 16 s period. In Figures 8a–8c, each red line represents either a positive or a negative component of a cross correlation and points in the direction from which the

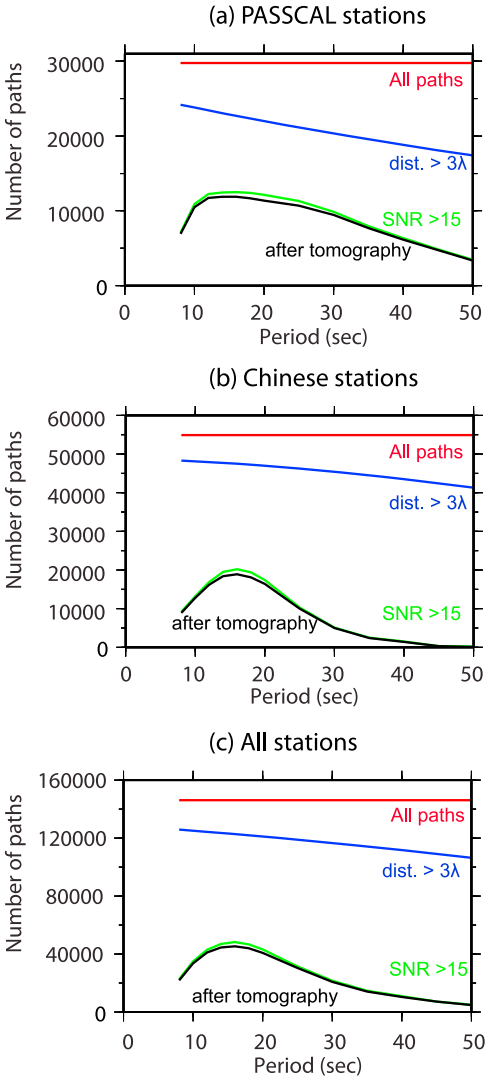

Figure 6. Number of data remaining after each step of data section, segregated by measurements (a) among PASSCAL stations, (b) among Chinese stations, and (c) among all stations. Following the same order of the three selection criteria, red lines represent the number of all measurements, blue lines represent the number remaining with interstation distances longer than three wavelengths, green lines represent the remaining number of measurements with SNR > 15, and black lines represent the remaining number of measurements that are fit to better than 7 s during tomography.

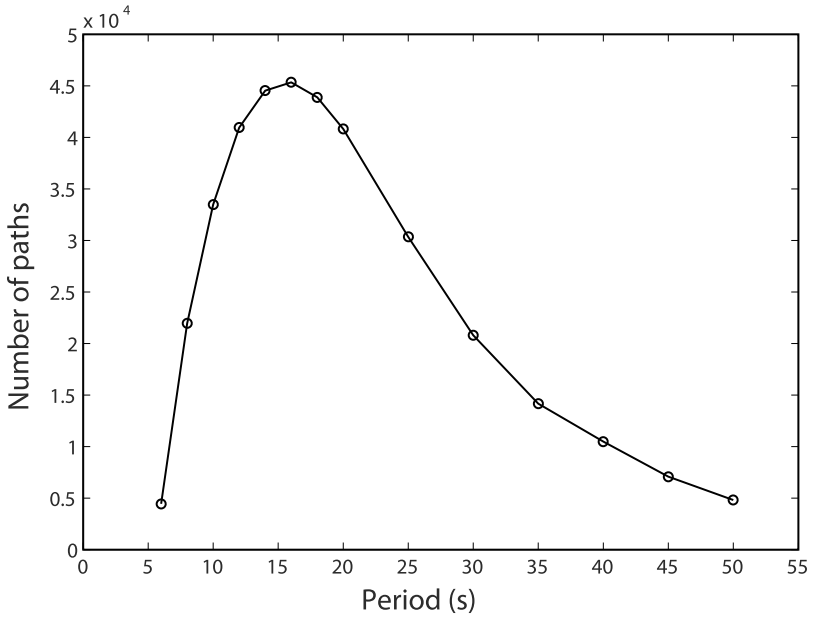

Figure 7. Number of selected final phase velocity measurements as a function of period.

energy arrives (i.e., it points to the source location). Each line's length is proportional to the SNR. The SNR of lines pointing toward the southern quadrant is highest, which means that strong ambient noise comes from the directions of the Indian Ocean and the western Pacific Ocean. The lowest SNR is observed toward the west, implying that the amplitude of ambient noise from the interior of the Eurasian plate

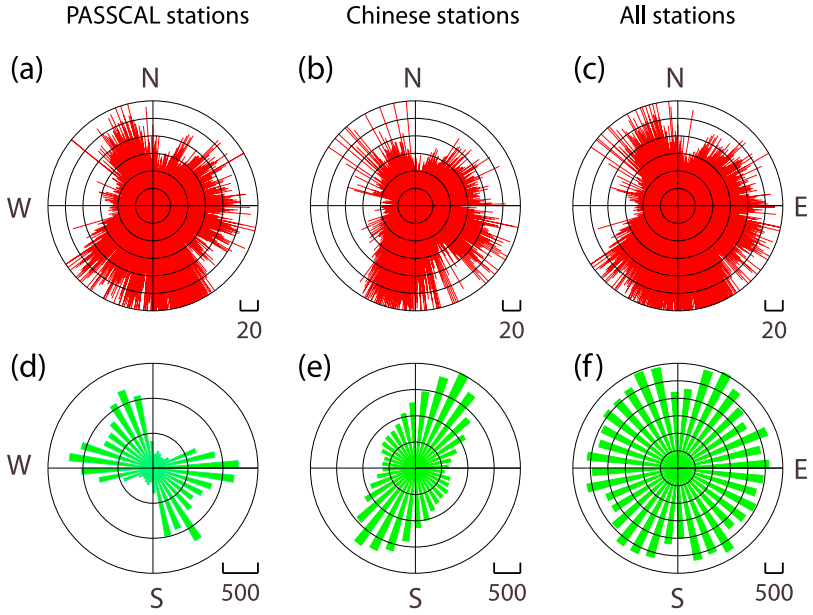

Figure 8. (a–c) Azimuthal distributions of SNR and (d–f) number of selected measurements at 16 s period, segregated among PASSCAL stations (Figures 8a and 8d), Chinese stations (Figures 8b and 8e), and all stations (Figures 8c and 8f). In Figures 8a–8c, each line represents either a positive or a negative component of a cross correlation and points in the direction from which the energy arrives (i.e., it points to the source location). Each line's length is proportional to the SNR, which is indicated by the concentric circles with the scale shown in the bottom right corner of each diagram. In Figures 8d–8f, each bar represents the number of selected paths calculated within each 10° azimuthal bin, and its number is indicated by the concentric circles with the scale shown in the bottom right corner of each diagram. Both azimuth and back azimuth are plotted in these diagrams.

is quite low. These observations are consistent with the argument by *Yang and Ritzwoller* [2008] that ambient noise comes dominantly from the directions of relatively nearby coastlines. In Figures 8d–8f, each bar's length represents the number of paths within each 10° azimuth bin. Both azimuth and back azimuth of each interstation path are included in Figure 8. For cross correlations exclusively among PASSCAL or Chinese stations, there are preferential directions for paths. A large number of paths among PASSCAL stations align in the NW–SE direction (Figure 8d) and a large number of paths among Chinese stations align in the NE–SW direction (Figure 8e). The variations of the number of paths with azimuth are mainly due to the spatial distributions of stations but are not due to azimuthal variations of the strength of ambient noise. For example, most of the Chinese stations are located along the NE–SW strike in the eastern part of our study region (Figure 1), which results in the observed large number of paths in this direction (Figure 8e). For measurements among all the stations (i.e., the total measurements used in the final surface wave tomography), the azimuthal distribution of paths is quite homogeneous and uniform (Figure 8f), which is good for resolution in surface wave tomography, particularly for extracting information about azimuthal anisotropy that will be pursued in a future study. These observations also highlight the advantage of ambient noise in providing homogenous ray coverage for surface wave tomography.

4. Phase Velocity Measurements and Surface Wave Tomography

[16] We measure phase velocity dispersion curves by automatic frequency-time analysis (FTAN). As illustrated by *Bensen et al.* [2007] and *Lin et al.* [2007], phase velocity measurements are much more accurate than group velocity measurements. Phase velocity is measured from instantaneous phase by reconciling the phase ambiguity. We follow *Lin et al.* [2007] to resolve the phase ambiguity by tracing phase velocity dispersion curves from long periods to short periods, because reference dispersion curves are more reliable at longer periods [e.g., *Shapiro and Ritzwoller*, 2002]. Some cross correlations, however, contain surface wave signals only at periods shorter than 40 s. To resolve this problem, we first perform a smoothed tomography using phase velocity dispersion measurements only from those cross correlations that have the longest period of surface wave signals greater than 40 s. With these dispersion measurements, we are able to construct smoothed phase velocity maps in a period range from 6 to 50 s. Using the resulting smoothed phase velocity maps as a new reference, we perform the FTAN on the remaining cross correlations containing only surface wave signals at periods shorter than 40 s to obtain the resulting dispersion curves.

[17] Figure 9 shows two examples of cross correlations and the corresponding phase velocity dispersion curves. The path between stations GS09 and EMS (red) lies mostly within the Sichuan Basin, and the path between stations D25 and MNI (blue) is within southeastern Tibet. Phase velocities at short periods (<12 s) in the Sichuan Basin are significantly lower than in southeastern Tibet because of the sediments in the Sichuan Basin. However, at periods longer than 12 s, phase velocities in the Sichuan Basin are much higher than in southeastern Tibet, indicating colder and stronger crust beneath the Sichuan Basin.

[18] Rayleigh wave phase velocity dispersion measurements are used to invert for phase velocity maps on a 1° × 1° spatial grid using the tomographic method of *Barmin et al.* [2001]. This method is based on minimizing a penalty functional composed of a linear combination of data misfit, model smoothness, and the perturbation to a reference model for isotropic wave velocity. The choice of the damping parameters is subjective, but we perform a number of tests using different combinations of parameters to determine reasonable values by considering data misfit, model resolution, and model smoothness.

[19] During tomography, resolution is also simultaneously estimated by using the method described by *Barmin et al.* [2001] with modifications presented by *Levshin et al.* [2005a]. Each row of the resolution matrix is a resolution surface (or kernel) for a specific grid node. We summarize the information of the resolution surface at each spatial node by fitting a 2-D symmetric spatial Gaussian function to the resolution surface at each node: $A\exp\left(-\frac{|r|^2}{2\gamma^2}\right)$. The spatial resolution at each node is defined as twice the standard deviation of this Gaussian function: γ. Examples of resolution maps and associated path coverage are plotted in Figure 10 for the 12 s, 30 s and 50 s period measurements. Resolution is estimated to be about 1° (~100 km) in the region to the east of 90.0°E where station coverage is very dense and 2–3° (~200–300 km) to the west of 90.0°E where stations are sparse. At long periods, the area with good path coverage shrinks and resolution reduces gradually due to the decrease in the number of measurements (Figure 7).

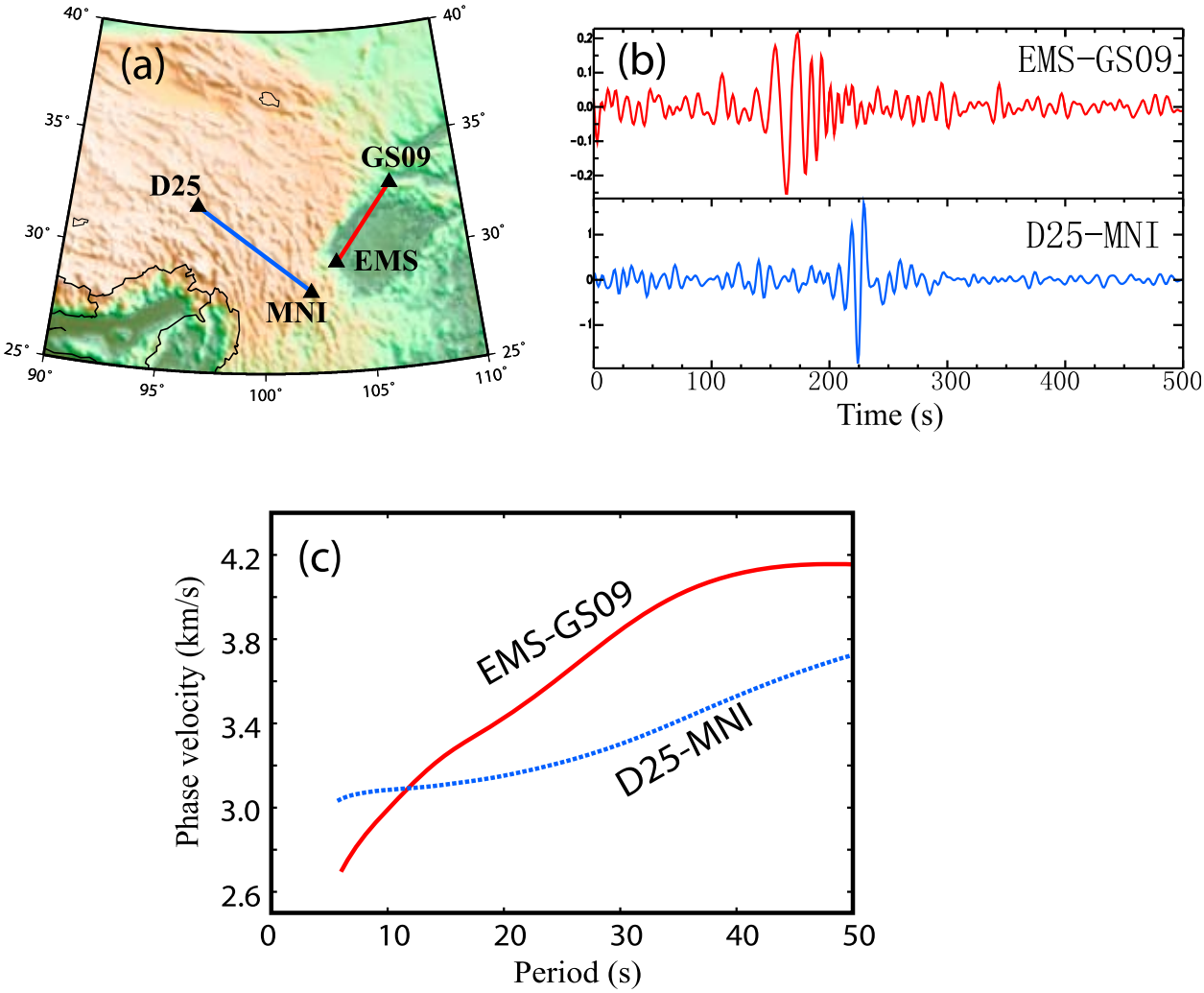

Figure 9. (a) Raypaths between stations EMS and GS09 (red) and between stations D25 and MNI (blue). (b) The 5–50 s band-pass filtered symmetric component cross correlations for the station pairs EMS-GS09 and D25–MNI. (c) The measured Rayleigh wave phase velocity dispersion curves based on the cross correlations shown in Figure 9b. The red curve is for the station pair EMS-GS09, and the blue curve for the station pair D25–MNI.

[20] Histograms of data misfits from the tomography at the three periods of 12, 25 and 40 s are plotted in Figure 11, segregated for measurements among PASSCAL stations, among Chinese stations, and among all stations. Misfits of measurements among PASSCAL stations and among Chinese stations are similar with nearly identical standard deviations of ~1.7 s. This means that the measurements that pass our selection criteria, particularly SNR > 15, obtained from the Chinese stations are probably as good as those from PASSCAL stations.

5. Phase Velocity Maps and Discussion

[21] Sample phase velocity maps at periods of 8, 12, 18, 25, 35 and 50 s are plotted in Figure 12 as perturbations relative to the average values at each individual period: 3.06 km/s, 3.11 km/s, 3.22 km/s, 3.35 km/s, 3.53 km/s, and 3.77 km/s, respectively. The features of the phase velocity maps vary gradually with period due to the overlap of the Rayleigh wave depth sensitivity kernels. The depth of maximum phase velocity sensitivity of Rayleigh waves to shear velocity is about one third of its wavelength. To guide qualitative interpretation, shear velocity sensitivity kernels of Rayleigh phase velocities are plotted in Figure 13. The 1-D Vs model used to construct the kernels is taken at (92.0°E, 32.0°N) from the 3-D model of *Shapiro and Ritzwoller* [2002]. Figure 14 presents the locations of some of the major geological and tectonic features observed in the Rayleigh phase velocity maps as well as a model of sediment thickness.

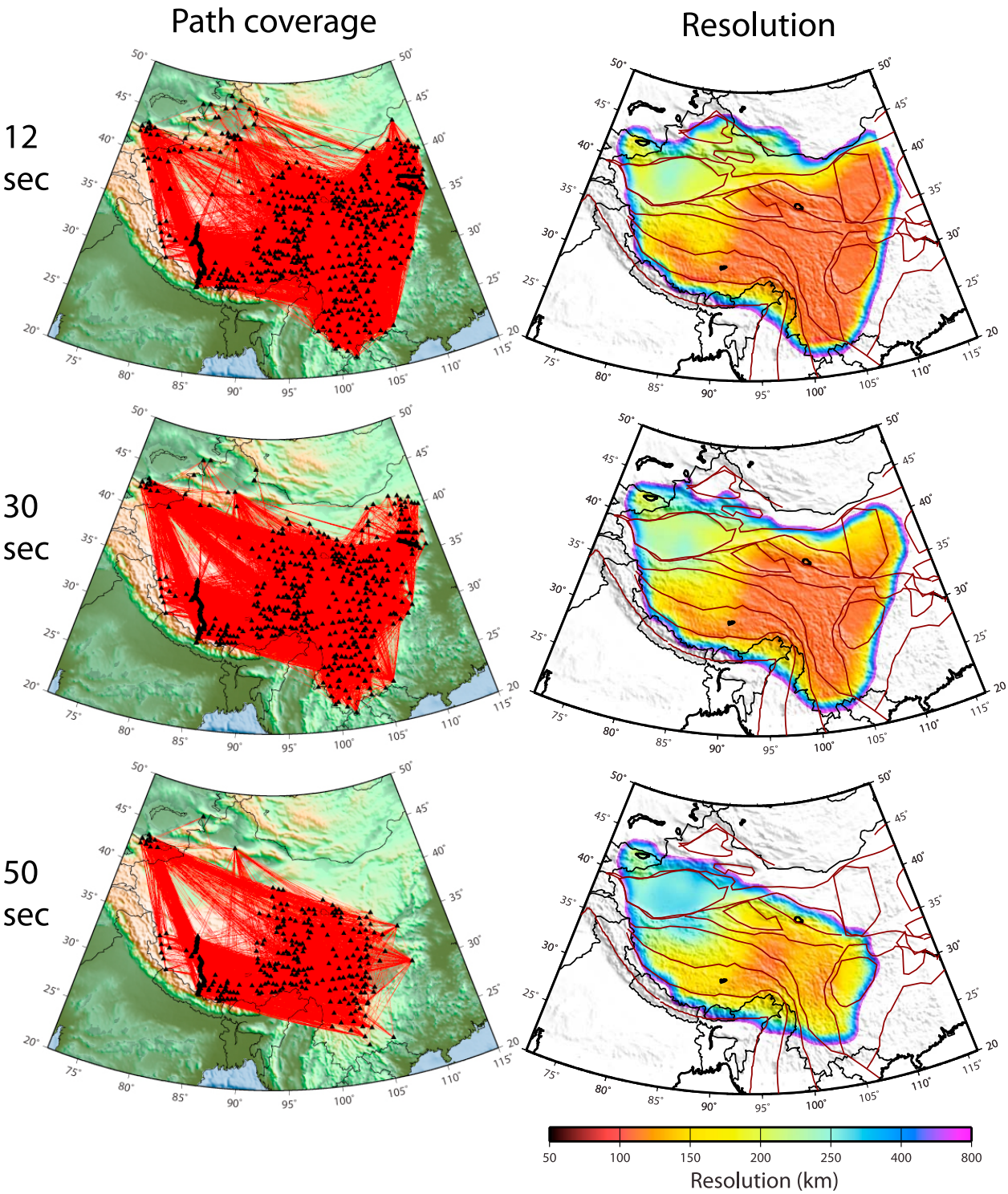

Figure 10. (left) Raypath coverage and (right) resolution maps at periods of 12, 30, and 50 s. Resolution is presented in units of kilometers and is defined as twice the standard deviation of a 2-D Gaussian fit to the resolution surface at each geographic node [e.g., *Barmin et al.*, 2001].

[22] At the short-period end of this study (6–14 s), phase velocities are dominantly sensitive to shear velocities in the upper crust. Because seismic velocities of sediments are much slower than those of crystalline rocks, sedimentary basins appear as short-period low-velocity anomalies. The 8 and 12 s phase velocity maps shown in Figures 12a and 12b clearly exhibit low velocities in the Tarim, Junggar,

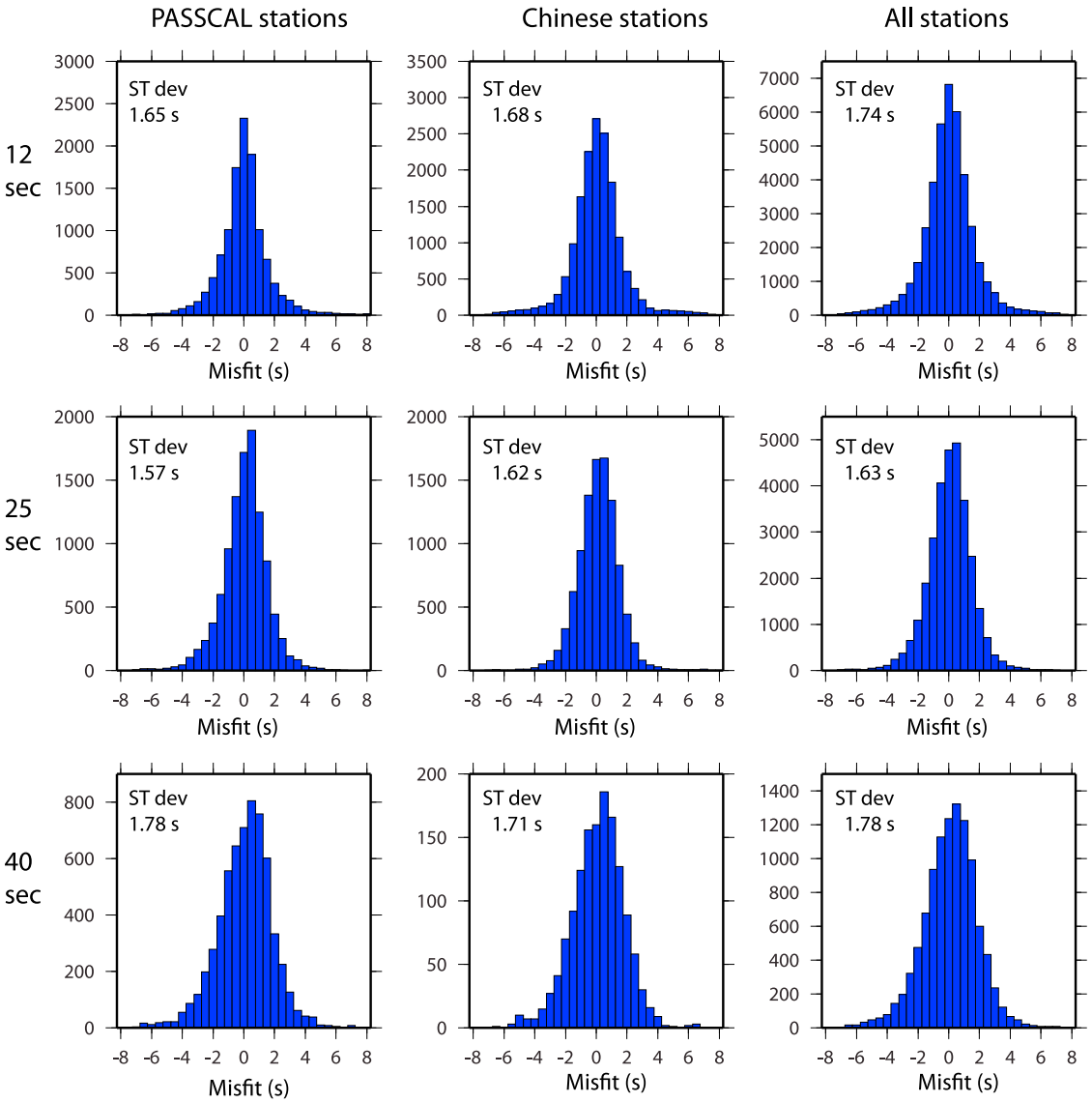

Figure 11. Histograms of data misfits at the three periods of (top) 12 s, (middle) 25 s, and (bottom) 40 s, segregated for measurements among (left) PASSCAL stations, (middle) Chinese stations, and (right) all stations. The corresponding standard deviation for each case is shown in each diagram.

Qadaim and Sichuan basins and also in the Ordos Block where sediments are present (Figure 14). At 18 s period, velocities in the Sichuan Basin and the Ordos Block become higher, while low velocities persist in the basins of Tarim, Junggar and Qadaim. This implies that sediment layers in the basins of Tarim, Junggar, Qadaim are thicker and/or sediment shear wave speeds are slower than those in the Sichuan Basin and the Ordos Block.

[23] At periods shorter than 20 s, velocities in the Tibetan Plateau appear lower than the surrounding nonbasin regions, indicating the upper crust in the Tibetan Plateau is warmer and weaker. Lower velocities in the Tibetan Plateau are also consistently observed at the intermediate and long periods (>25 s), which is in part due to the very thick crust of the Tibetan Plateau (>65 km).

[24] At long periods (>30 s), Rayleigh waves become primarily sensitive to crustal thickness and the shear velocities in the lower crust and uppermost mantle (Figure 13). The phase velocity maps at periods from 25 to 50 s are inversely correlated with crustal thickness, with high velocities in regions with thin crust and low velocities in regions with thick crust (Figures 12c–12e). Very high velocity anomalies at 25–50 s periods are centered in the Tarim Basin, the Ordos Block and the Sichuan Basin, especially pronounced at 35 s period

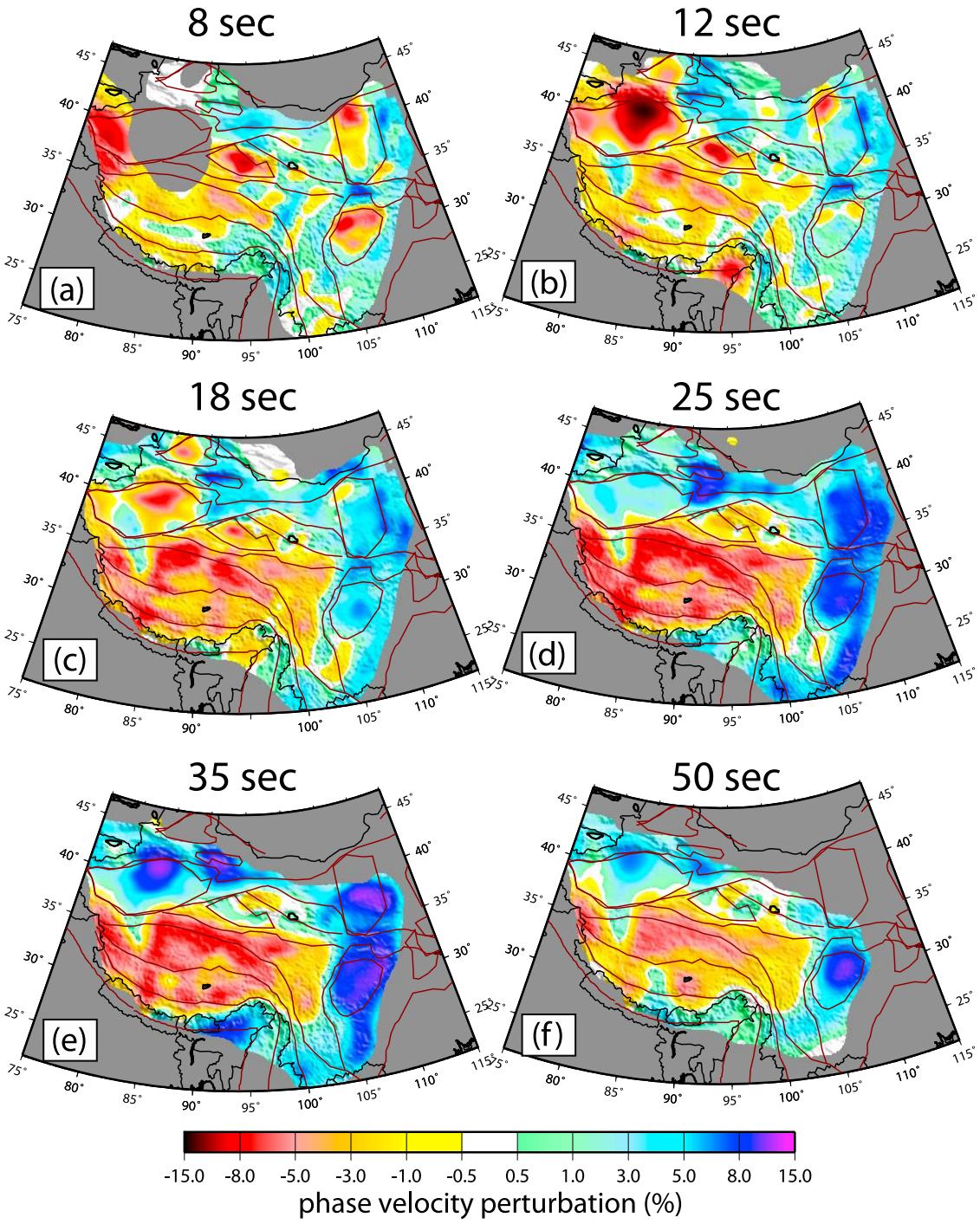

Figure 12. Phase velocity maps at periods of (a) 8, (b) 12, (c) 18, (d) 25, (e) 35, and (f) 50 s. Phase velocities are plotted as perturbations relative to the average value at each period. The maps truncate (reduce to gray shades) in regions where the resolution is worse than 400 km.

(Figure 12e). Low velocities observed in eastern Tibet appear to bifurcate west of the Sichuan Basin, similar to the study of *Li et al.* [2009]. The low phase velocities across the Tibetan Plateau at 25–50 s periods alone cannot be interpreted directly as a low-velocity layer in the middle or lower crust because low phase velocities in northern Tibet could be the result of the uniformly thickened crust in northern Tibet. Low shear wave velocities in the middle crust were previously confirmed to exist only in southern Tibet, west of 92°E [*Cotte et al.*, 1999; *Rapine et al.*, 2003; *Caldwell et al.*, 2009]. Systematic

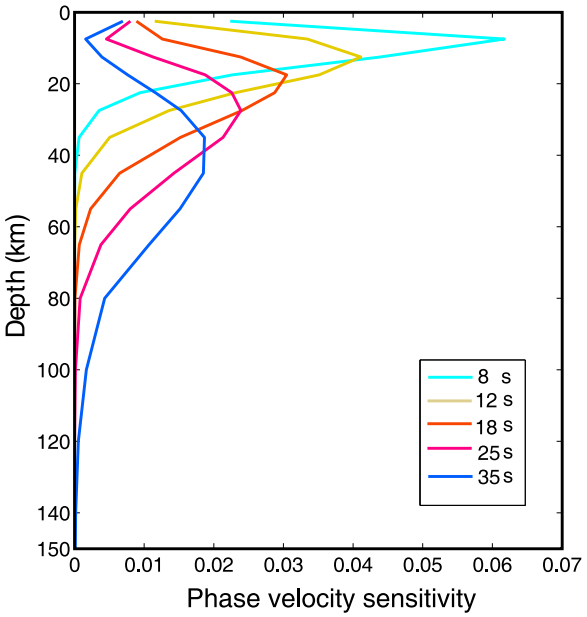

Figure 13. Shear velocity sensitivity kernels of Rayleigh phase velocities at 8, 12, 18, 25, 35, and 50 s.

interpretation of low velocity anomalies throughout Tibet awaits the inversion for a 3-D shear velocity model in a future study.

[25] Within the Tibetan Plateau, there are also significant velocity variations. The most pronounced anomalies are lower velocities observed in northern Tibet within the western Qangtang and Songpan-Ganze terranes. These low velocities appear consistently over the whole period range from 8 to 50 s with the lowest-velocity anomalies observed at intermediate periods from 20 to 40 s. The locations of these low-velocity anomalies are coincident with the distribution of Mid-Miocene to Quaternary volcanic rocks [*Arnaud et al.*, 1992; *Turner et al.*, 1993, 1996; *Guo et al.*, 2006] in northern Tibet, which suggests that the crust and uppermost mantle in northern Tibet is very hot and could contain partial melt where velocities are lowest. The imaged low phase velocities are consistent with low Pn velocities observed in the Qangtan and Songpan-Ganze terranes by *Liang and Song* [2006] and also correlate with the observations of inefficient Sn propagation believed to be due to high temperatures in the uppermost mantle [*Ni and Barazangi*, 1983; *McNamara et al.*, 1995]. The apparent phase velocity variations in the Tibetan Plateau imply that the high elevation and thick crust of the plateau may be created and maintained in different ways with spatial and perhaps temporal variations [e.g., *Owens and Zandt*, 1997] even though the topography is nearly uniform across the entire Tibetan Plateau.

[26] Several small patches of low velocities at intermediate periods (20–40 s) in southern Tibet are also imaged (Figures 12d and 12e). The locations of these low velocities are mostly coincident with the

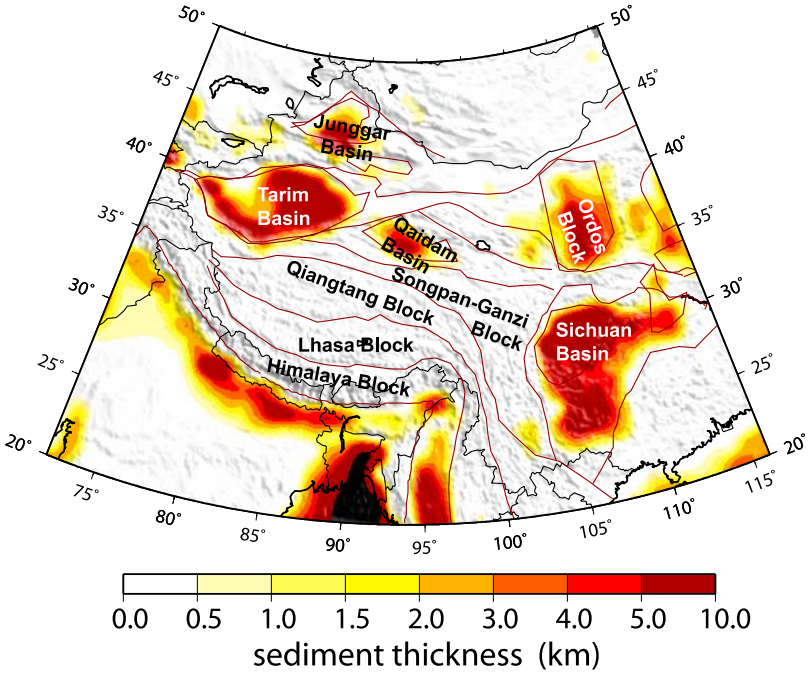

Figure 14. Map of sediment thickness taken from CRUST2.0 [*Bassin et al.*, 2000]. The locations of major geological units discussed in the text are marked approximately.

rift zones in southern Tibet, implying that rifts observed at the surface may be related to low velocities in the middle to upper lower crust and have a deep-seated origin. This is consistent with the observations from seismic refraction surveys [*Cogan et al.*, 1998]. Based on magnetotelluric data from the Tibetan–Himalayan orogen, *Unsworth et al.* [2005] find very low resistivity present in the middle crust in the southern margin of the Tibetan plateau. Because electrical resistivity is sensitive to the presence of interconnected fluids in the host rock matrix, they interpret the low-resistivity zone as a partially molten layer. Our observed low velocities at intermediate periods in southern Tibet may also reflect a partially molten layer.

[27] A small patch of high velocities appears in northwestern Tibet at 12–50 s periods. This high-velocity anomaly is aligned in the NW–SE direction, which is also the bearing direction of the majority of raypaths (Figure 10). This high-velocity feature may be due to smearing of high velocities from the Tarim Basin and/or in the western Tian Shan toward northwestern Tibet.

6. Summary

[28] We apply ambient noise tomography to significant data resources available across Tibet and the surrounding regions, including seismic stations from the permanent Federation of Digital Seismographic Networks (FDSN), several temporary U.S. PASSCAL installations in and around Tibet, and the Chinese provincial networks surrounding Tibet. These networks comprise about 600 stations, which yield between 5000 and 45000 high-quality dispersion measurements depending on period and provide unprecedented path coverage across the entire Tibetan Plateau. We devote considerable effort to data quality control by checking instrument responses, comparing the two-sided arrivals in the cross correlations, comparing SNR and analyzing data coherence during tomography. Data quality from Chinese stations is overall lower than that from PASSCAL stations because PASSCAL stations are equipped with true broadband sensors. However, dispersion measurements that pass the three selection criteria (interstation distance, SNR, and data coherence) obtained from the Chinese stations are as good as those from PASSCAL stations. Ambient noise cross correlations are performed on these networks from 2003 to 2009. Interstation Rayleigh wave phase dispersion curves at periods from 6 to 50 s are measured from cross correlations of vertical components and then used to invert for Rayleigh phase velocity maps.

[29] The resulting phase velocity maps have resolutions between 100 and 200 km across most of the Tibetan Plateau and reveal a wealth of velocity features associated with tectonic structures. Rayleigh phase velocity maps at short periods show strong low-velocity anomalies correlated with the major sedimentary basins of Tarim, Junggar, Qaidam and Sichuan and the Ordos Block. At intermediate and long periods (>25 s), high-velocity anomalies are observed in the Tarim Basin, the Ordos Block and the Sichuan Basin. Phase velocities in the Tibetan Plateau are lower than in the surrounding regions. Phase velocities in northern Tibet are lower than in southern Tibet.

Acknowledgments

[30] The facilities of the IRIS Data Management System, and specifically the IRIS Data Management Center, were used for access to waveforms and metadata of all the PASSCAL and FDSN stations required in this study. We thank all the PIs and team members of the PASSCAL experiments and staff from the PASSCAL Instrument Center for collecting valuable data in Tibet. We thank the Network Center of Chinese Earthquake Administration for providing us with the Chinese data. We also thank Hongyi Li and another anonymous reviewer for their constructive comments. This work is supported by NSF-EAR award 0944022 and a subaward from NSF-OISE 0730154. Yong Zheng is supported by a Chinese National Science Foundation award, 40974034, and a Chinese Academy of Sciences grant, CAS Y009021002. The INDEPTH-IV passive source team was supported by both China (grants 4052012222 and 480821062) and the U.S. National Science Foundation under grants EAR-0634903 and EAR-0409589.

References

Arnaud, N. O., P. Vidal, P. Tapponnier, P. Matte, and W. M. Deng (1992), The High K2O volcanism of northwestern Tibet—Geochemistry and tectonic implications, *Earth Planet. Sci. Lett.*, *111*, 351–367, doi:10.1016/0012-821X(92)90189-3.

Barmin, M. P., M. H. Ritzwoller, and A. L. Levshin (2001), A fast and reliable method for surface wave tomography, *Pure Appl. Geophys.*, *158*, 1351–1375, doi:10.1007/PL00001225.

Bassin, C., G. Laske, and G. Masters (2000), The current limits of resolution for surface wave tomography in North America, *Eos Trans AGU*, *81*(48), Fall Meet. Suppl., Abstract S12A-03.

Bensen, G. D., M. H. Ritzwoller, M. P. Barmin, A. L. Levshin, F. Lin, M. P. Moschetti, N. M. Shapiro, and Y. Yang (2007), Processing seismic ambient noise data to obtain reliable broad-band surface wave dispersion measurements, *Geophys. J. Int.*, *169*, 1239–1260.

Bensen, G. D., M. H. Ritzwoller, and N. M. Shapiro (2008), Broadband ambient noise surface wave tomography across

the United States, *J. Geophys. Res.*, *113*, B05306, doi:10.1029/2007JB005248.

Bensen, G. D., M. H. Ritzwoller, and Y. Yang (2009), A 3-D shear velocity model of the crust and uppermost mantle beneath the United States from ambient seismic noise, *Geophys. J. Int.*, *177*, 1177–1196, doi:10.1111/j.1365-246X.2009.04125.x.

Caldwell, W. B., S. L. Klemperer, S. S. Rai, and J. F. Lawrence (2009), Partial melt in the upper-middle crust of the northwest Himalayas revealed by Rayleigh wave dispersion, *Tectonophysics*, *477*, 58–65, doi:10.1016/j.tecto.2009.01.013.

Cho, K. H., R. B. Herrmann, C. J. Ammon, and K. Lee (2007), Imaging the upper crust of the Korean Peninsula by surface-wave tomography, *Bull. Seismol. Soc. Am.*, *97*, 198–207, doi:10.1785/0120060096.

Cogan, M. J., K. D. Nelson, W. S. F. Kidd, C. Wu, and the Project Indepth Team (1998), Shallow structure of the Yadong-Gulu rift, southern Tibet, from refraction analysis of Project INDEPTH common midpoint data, *Tectonics*, *17*, 46–61, doi:10.1029/97TC03025.

Cotte, N., H. Pedersen, M. Campillo, J. Mars, J. F. Ni, R. Kind, E. Sandvol, and W. Zhao (1999), Determination of the crustal structure in southern Tibet by dispersion and amplitude analysis of Rayleigh waves, *Geophys. J. Int.*, *138*(3), 809–819.

Friederich, W. (2003), The S-velocity structure of the East Asian mantle from inversion of shear and surface waveforms, *Geophys. J. Int.*, *153*, 88–102, doi:10.1046/j.1365-246X.2003.01869.x.

Guo, Z., M. Wilson, J. Liu, and Q. Mao (2006), Post-collisional, potassic and ultrapotassic magmatism of the Northern Tibetan Plateau: Constraints on characteristics of the mantle source, geodynamic setting and uplift mechanisms, *J. Petrol.*, *47*, 1177–1220, doi:10.1093/petrology/egl007.

Guo, Z., X. Gao, H. Yao, J. Li, and W. Wang (2009), Midcrustal low-velocity layer beneath the central Himalaya and southern Tibet revealed by ambient noise array tomography, *Geochem. Geophys. Geosyst.*, *10*, Q05007, doi:10.1029/2009GC002458.

Huang, Z. X., W. Su, Y. J. Peng, Y. J. Zheng, and H. Y. Li (2003), Rayleigh wave tomography of China and adjacent regions, *J. Geophys. Res.*, *108*(B2), 2073, doi:10.1029/2001JB001696.

Levshin, A. L., M. H. Ritzwoller, and L. I. Ratnikova (1994), The nature and cause of polarization anomalies of surface-wave crossing northern and central Eurasia, *Geophys. J. Int.*, *117*, 577–590, doi:10.1111/j.1365-246X.1994.tb02455.x.

Levshin, A. L., M. P. Barmin, M. H. Ritzwoller, and J. Trampert (2005a), Minor-arc and major-arc global surface wave diffraction tomography, *Phys. Earth Planet. Inter.*, *149*, 205–223, doi:10.1016/j.pepi.2004.10.006.

Levshin, A. L., M. H. Ritzwoller, and N. M. Shapiro (2005b), The use of crustal higher modes to constrain crustal structure across central Asia, *Geophys. J. Int.*, *160*, 961–972, doi:10.1111/j.1365-246X.2005.02535.x.

Li, H. Y., W. Su, C. Y. Wang, and Z. X. Huang (2009), Ambient noise Rayleigh wave tomography in western Sichuan and eastern Tibet, *Earth Planet. Sci. Lett.*, *282*, 201–211, doi:10.1016/j.epsl.2009.03.021.

Liang, C. T., and X. D. Song (2006), A low velocity belt beneath northern and eastern Tibetan Plateau from Pn tomography, *Geophys. Res. Lett.*, *33*, L22306, doi:10.1029/2006GL027926.

Lin, F. C., M. H. Ritzwollerl, J. Townend, S. Bannister, and M. K. Savage (2007), Ambient noise Rayleigh wave tomography of New Zealand, *Geophys. J. Int.*, *170*, 649–666, doi:10.1111/j.1365-246X.2007.03414.x.

Lin, F. C., M. P. Moschetti, and M. H. Ritzwoller (2008), Surface wave tomography of the western United States from ambient seismic noise: Rayleigh and Love wave phase velocity maps, *Geophys. J. Int.*, *173*, 281–298, doi:10.1111/j.1365-246X.2008.03720.x.

McNamara, D. E., T. J. Owens, and W. R. Walter (1995), Observations of regional phase propagation across the Tibetan Plateau, *J. Geophys. Res.*, *100*, 22,215–22,229, doi:10.1029/95JB01863.

Moschetti, M. P., M. H. Ritzwoller, and N. M. Shapiro (2007), Surface wave tomography of the western United States from ambient seismic noise: Rayleigh wave group velocity maps, *Geochem. Geophys. Geosyst.*, *8*, Q08010, doi:10.1029/2007GC001655.

Nelson, K. D., et al. (1996), Partially molten middle crust beneath southern Tibet: Synthesis of Project INDEPTH results, *Science*, *274*, 1684–1688.

Ni, J., and M. Barazangi (1983), Velocities and propagation characteristics of Pn, Pg, Sn, and Lg seismic waves beneath the Indian Shield, Himalayan Arc, Tibetan Plateau, and surrounding regions: High uppermost mantle velocities and efficient Sn propagation beneath Tibet, *Geophys. J. R. Astron. Soc.*, *72*, 665–689.

Nishida, K., H. Kawakatsu, and K. Obara (2008), Three-dimensional crustal *S* wave velocity structure in Japan using microseismic data recorded by Hi-net tiltmeters, *J. Geophys. Res.*, *113*, B10302, doi:10.1029/2007JB005395.

Owens, T. J., and G. Zandt (1997), Implications of crustal property variations for models of Tibetan plateau evolution, *Nature*, *387*, 37–43, doi:10.1038/387037a0.

Priestley, K., E. Debayle, D. McKenzie, and S. Pilidou (2006), Upper mantle structure of eastern Asia from multimode surface waveform tomography, *J. Geophys. Res.*, *111*, B10304, doi:10.1029/2005JB004082.

Rapine, R., F. Tilmann, M. West, J. Ni, and A. Rogers (2003), Crustal structure of northern and southern Tibet from surface wave dispersion analysis, *J. Geophys. Res.*, *108*(B2), 2120, doi:10.1029/2001JB000445.

Ritzwoller, M. H., and A. L. Levshin (1998), Eurasian surface wave tomography: Group velocities, *J. Geophys. Res.*, *103*, 4839–4878, doi:10.1029/97JB02622.

Ritzwoller, M. H., A. L. Levshin, L. I. Ratnikova, and A. A. Egorkin (1998), Intermediate-period group-velocity maps across central Asia, western China and parts of the Middle East, *Geophys. J. Int.*, *134*, 315–328.

Royden, L. H., B. C. Burchfiel, R. W. King, E. Wang, Z. L. Chen, F. Shen, and Y. P. Liu (1997), Surface deformation and lower crustal flow in eastern Tibet, *Science*, *276*, 788–790, doi:10.1126/science.276.5313.788.

Sabra, K. G., P. Gerstoft, P. Roux, W. A. Kuperman, and M. C. Fehler (2005), Surface wave tomography from microseisms in Southern California, *Geophys. Res. Lett.*, *32*, L14311, doi:10.1029/2005GL023155.

Saygin, E., and B. L. N. Kennett (2010), Ambient seismic noise tomography of Australian continent, *Tectonophysics*, *481*, 116–125, doi:10.1016/j.tecto.2008.11.013.

Shapiro, N. M., and M. H. Ritzwoller (2002), Monte-Carlo inversion for a global shear-velocity model of the crust and upper mantle, *Geophys. J. Int.*, *151*, 88–105, doi:10.1046/j.1365-246X.2002.01742.x.

Shapiro, N. M., M. H. Ritzwoller, P. Molnar, and V. Levin (2004), Thinning and flow of Tibetan crust constrained by

seismic anisotropy, *Science*, *305*, 233–236, doi:10.1126/science.1098276.

Shapiro, N. M., M. Campillo, L. Stehly, and M. H. Ritzwoller (2005), High-resolution surface-wave tomography from ambient seismic noise, *Science*, *307*, 1615–1618, doi:10.1126/science.1108339.

Stehly, L., M. Campillo, and N. M. Shapiro (2007), Traveltime measurements from noise correlation: Stability and detection of instrumental time-shifts, *Geophys. J. Int.*, *171*, 223–230, doi:10.1111/j.1365-246X.2007.03492.x.

Turner, S., C. Hawkesworth, J. Q. Liu, N. Rogers, S. Kelley, and P. Vancalsteren (1993), Timing of Tibetan uplift constrained by analysis of volcanic rocks, *Nature*, *364*, 50–54, doi:10.1038/364050a0.

Turner, S., N. Arnaud, J. Liu, N. Rogers, C. Hawkesworth, N. Harris, S. Kelley, P. Van Calsteren, and W. Deng (1996), Post-collision, shoshonitic volcanism on the Tibetan plateau: Implications for convective thinning of the lithosphere and the source of ocean island basalts, *J. Petrol.*, *37*, 45–71, doi:10.1093/petrology/37.1.45.

Unsworth, M. J., et al. (2005), Crustal rheology of the Himalaya and Southern Tibet inferred from magnetotelluric data, *Nature*, *438*, 78–81, doi:10.1038/nature04154.

Villaseñor, A., M. H. Ritzwoller, A. L. Levshin, M. P. Barmin, E. R. Engdahl, W. Spakman, and J. Trampert (2001), Shear velocity structure of central Eurasia from inversion of surface wave velocities, *Phys. Earth Planet. Inter.*, *123*, 169–184, doi:10.1016/S0031-9201(00)00208-9.

Villaseñor, A., Y. Yang, M. H. Ritzwoller, and J. Gallart (2007), Ambient noise surface wave tomography of the Iberian Peninsula: Implications for shallow seismic structure, *Geophys. Res. Lett.*, *34*, L11304, doi:10.1029/2007GL030164.

Yang, Y. J., and M. H. Ritzwoller (2008), Characteristics of ambient seismic noise as a source for surface wave tomography, *Geochem. Geophys. Geosyst.*, *9*, Q02008, doi:10.1029/2007GC001814.

Yang, Y., M. Ritzwoller, A. Levshin, and N. Shapiro (2007), Ambient noise Rayleigh wave tomography across Europe, *Geophys. J. Int.*, *168*, 259–274, doi:10.1111/j.1365-246X.2006.03203.x.

Yang, Y. J., A. B. Li, and M. H. Ritzwoller (2008a), Crustal and uppermost mantle structure in southern Africa revealed from ambient noise and teleseismic tomography, *Geophys. J. Int.*, *174*, 235–248, doi:10.1111/j.1365-246X.2008.03779.x.

Yang, Y. J., M. H. Ritzwoller, F. C. Lin, M. P. Moschetti, and N. M. Shapiro (2008b), Structure of the crust and uppermost mantle beneath the western United States revealed by ambient noise and earthquake tomography, *J. Geophys. Res.*, *113*, B12310, doi:10.1029/2008JB005833.

Yao, H. J., R. D. van der Hilst, and M. V. de Hoop (2006), Surface-wave array tomography in SE Tibet from ambient seismic noise and two-station analysis—I. Phase velocity maps, *Geophys. J. Int.*, *166*, 732–744, doi:10.1111/j.1365-246X.2006.03028.x.

Yao, H., C. Beghein, and R. D. Van der Hilst (2008), Surface-wave array tomography in SE Tibet from ambient seismic noise and two-station analysis: II—Crustal and upper mantle structure, *Geophys. J. Int.*, *173*(1), 205–219, doi:10.1111/j.1365-246X.2007.03696.x.

Zheng, S. H., X. L. Sun, X. D. Song, Y. J. Yang, and M. H. Ritzwoller (2008), Surface wave tomography of China from ambient seismic noise correlation, *Geochem. Geophys. Geosyst.*, *9*, Q05020, doi:10.1029/2008GC001981.